ORNL/sub/87-SA946/07

Properties and Performance of Ceramic Composite Components

August 9, 1999

Report Prepared by
S. W. Case, H. G. Halverson, R. H. Carter, M. Wone, and K. L. Reifsnider
Department of Engineering Science and Mechanics
Virginia Polytechnic Institute and State University
Blacksburg, VA 24061

under
Subcontract Number 19X-SA496C

for

OAK RIDGE NATIONAL LABORATORY
Oak Ridge, Tennessee 37831
Managed by
LOCKHEED MARTIN ENERGY RESEARCH CORP.
for the
U. S. DEPARTMENT OF ENERGY
under contract DE-AC05-96OR22464

DISCLAIMER

DISCLAIMER

Portions of this document may be illegible in electronic image products. Images are produced from the best available original document.

ORNL/sub/87-SA946/07

Properties and Performance of Ceramic Composite Components

August 9, 1999

Report Prepared by
S. W. Case, H. G. Halverson, R. H. Carter, M. Wone, and K. L. Reifsnider
Department of Engineering Science and Mechanics
Virginia Polytechnic Institute and State University
Blacksburg, VA 24061

under
Subcontract Number 19X-SA496C

for

OAK RIDGE NATIONAL LABORATORY
Oak Ridge, Tennessee 37831
Managed by
LOCKHEED MARTIN ENERGY RESEARCH CORP.
for the
U. S. DEPARTMENT OF ENERGY
under contract DE-AC05-96OR22464

TABLE OF CONTENTS

1. Introduction[†]

The objective of the Fossil Energy Advanced Research and Technology Development (AR&TD) Materials program is to conduct research and development on materials for longer-term fossil energy applications as well as for generic needs of various fossil fuel technologies. These needs have prompted research aimed toward a better understanding of material behavior in fossil energy environments and the development of new materials capable of substantial enhancement of plant operations, reliability, and efficiency.

The research program of the Materials Response Group at Virginia Tech addresses the need for reliable and durable ceramic composites to perform in high temperature applications. Two of the major fossil energy applications for ceramic matrix composites are heat exchangers and hot-gas filters.[1,2] In Section 2, we discuss the mechanical property characterization of oxide/oxide hot gas candle filters. This characterization includes tensile response, as well as response to internal pressurization. In Section 3, we discuss the characterization of dense Nextel/SiC structural tubes. In this study, the tube responses to axial tensile and compression loading as well as to torsional loading are measured.

In addition to these experimental characterizations of composite performance, we have also been involved in a number of modeling activities that are of importance for relating the behavior of the composite to the behavior of the constituents. The first of these modeling activities (described in Section 4) is to develop an understanding of the bridging stresses in cracks that extend into both 0° and 90° plies. The stress concentrations that result in the 0° plies may be important for making accurate predictions of the tensile strength of cross-plied and woven laminates. Also, we have been working toward the goal of developing models for the strength and toughness of fibril-reinforced composites. The first step toward this goal, described in Section 5, is to develop models for the bridging stresses in cases in which the bridging fibers are randomly oriented.

In the last modeling effort described in Section 6, we attempt to join two types of durability models that include the effects of multiple degradation mechanisms: those based upon detailed micromechanical simulations of the composite behavior and those based upon remaining strength. To do so, we use the results from the micromechanical simulations for single degradation mechanisms acting independently as inputs to the remaining strength model. The remaining strength model is then used to predict the combined behavior and the results compared to those from the numerical simulation.

[†] Research sponsored by the U. S. Department of Energy, Fossil Energy Advanced Research and Technology Development Materials Program, DOE/FE AA 15 10 10 0, Work Breakdown Structure Element VPI-1

2. Performance of Hot Gas Candle Filters

Removal of particulate from hot gas streams is a current source of energy loss in power generation. Current systems require the gas to be cooled before filtration or separation, resulting in an overall reduction of efficiency. Service conditions dictate that the filters must be able to endure sustained exposure to high temperatures, caustic environments, and severe thermal shock. Research into high temperature systems that operate without the need to cool the gas stream has produced several different candidate systems. These range from monolithic ceramics to a variety of ceramic composite structures. Several papers have been written reporting on the performance of the different materials and structures[3,4,5]. They use a variety of different test procedures to characterize these materials. Axial tension, O and C-ring tension and compression, and internal pressure tests are frequently chosen to characterize the stiffness and strength changes with high temperature/service condition exposure. However, the O and C-ring tests generate complex stress states over a small volume of material and therefore do not lend themselves to accurate calculation of the global properties. Therefore, in this study, axial tension and compression, torsion and internal pressure tests are performed to provide a complete test matrix for determining the global stiffness and strengths.

This research is being performed on the candidate filter supplied by McDermott Technologies, Inc. of Lynchburg, Virginia. This is an oxide/oxide ceramic composite design. The structure is a Nextel 610 fiber filament wound to form the backbone. The matrix is composed of chopped Saffil fibers that are added during the filament winding procedure. The two types of fiber are bonded together by an aluminum oxide layer deposited by sol-gel processing. This produces a structure with the high porosity (~70%) and small pore size needed for the filter.

The objective of this research is to test the McDermott filter material, characterizing the mechanical response under several loading conditions and after exposure to high temperature and severe thermal shock. Several samples have been exposed to different degrees of simulated back pulses (where ambient temperature air is forced back through the 800°C filter to remove any particulate buildup on the outer surface). The tests described in this paper were selected to create a complete data set such that it would lend itself to composite material analysis. This will increase the understanding of the damage and material degradation modes. The experimental results are used to validate different modeling approaches. The ultimate goal is to apply the experimental results and models to generate life prediction estimates.

2.1 Axial tests

A schematic of the axial test samples is in Figure 1A. Elastic stiffness was measured on tube sections with a 12.5-cm gage section. Tests were performed on a MTS servo-hydraulic load frame with axial and torsional capabilities. A mounting fixture gripped the pins placed through the ends of the tube. Two different methods were used to minimize the effect of the pinholes. First, a ceramic foam plug, cut to match the inner

diameter of the tube, was bonded around the pin and inner surface to distribute the load away from the hole. This proved to be insufficient, so a second method of potting the end in epoxy was used.

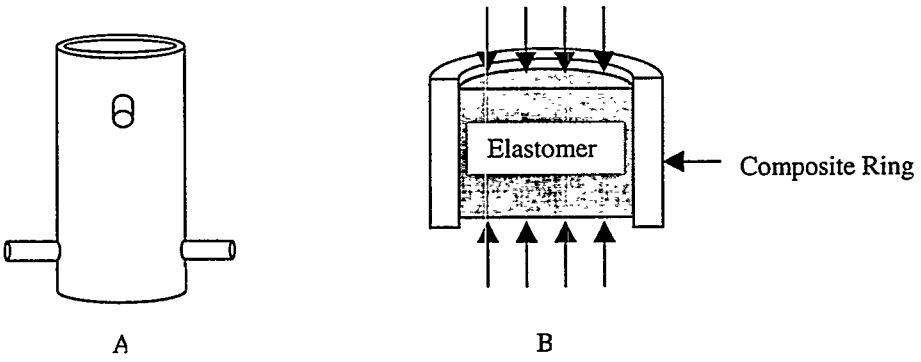

Figure 1: Schematic of test samples. A) Axial test sample. B) Internal pressure test sample.

The axial tension and compression tests have a limit of 450 N (~100 lbs.) tension and 225 N (~50 lbs.) compression. The torsional stiffness test range was ±115 N-m (~100 in-lbs.). Surface strain was measured using strain gages and extensometers.

Axial stiffness calculations are based on the extensometer measurements. Strain gage data are on the order of 15% stiffer than the extensometer measurements due to the adhesive permeating and locally reinforcing the matrix. This is not believed to have a significant affect on the torsional stiffness measurements. It has been shown using an energy formulation of the displacement of a composite tube that the axial stiffness is predominantly controlled by the matrix properties, while the torsional stiffness is more closely related to that of the reinforcing fiber properties[2]. This is not unexpected since the material is a ±45° woven structure. Another concern during testing is how minor specimen misalignment can lead to significant bending moments. To account for resulting bending moments, all strain measurements were made at four locations, equally spaced around the tube. Averaging the data removed the resulting linear offset and gave an accurate measurement of stiffness.

Axial and torsional stiffness results are in Figures 2 and 3. At this point, little to no degradation of axial stiffness can be attributed to back-pulse exposure. More samples, especially those subjected to 10 and 100 thousand back-pulse cycles, are currently being tested.

Tensile stress-strain curves are shown in Figure 4. Samples 3 and 4 utilized the ceramic end plug, while 7 and 8 were potted in epoxy. The reduction in strength is due to a change in the failure mode. The samples using a ceramic end plug bonded to the inner surface failed with cracks originating at the pinholes and winding around the sample following the fiber tows. The samples with the epoxy ends underwent a gradual failure with gage section necking. Due to the change in the mounting, it is impossible to attribute changes in the fracture stress to back pulse exposure. Currently, more samples with the epoxy end plugs are being tested so variations in tensile strength can be attributed to

service exposure. For the samples mounted with epoxy, the material exhibited no large crack formation at the maximum strain level (4-6% strain or 4-6 mm displacement), but generated damage throughout the sample. There appeared to be no fiber failure, instead matrix failure, shear band formation and fiber realignment are the primary failure modes.

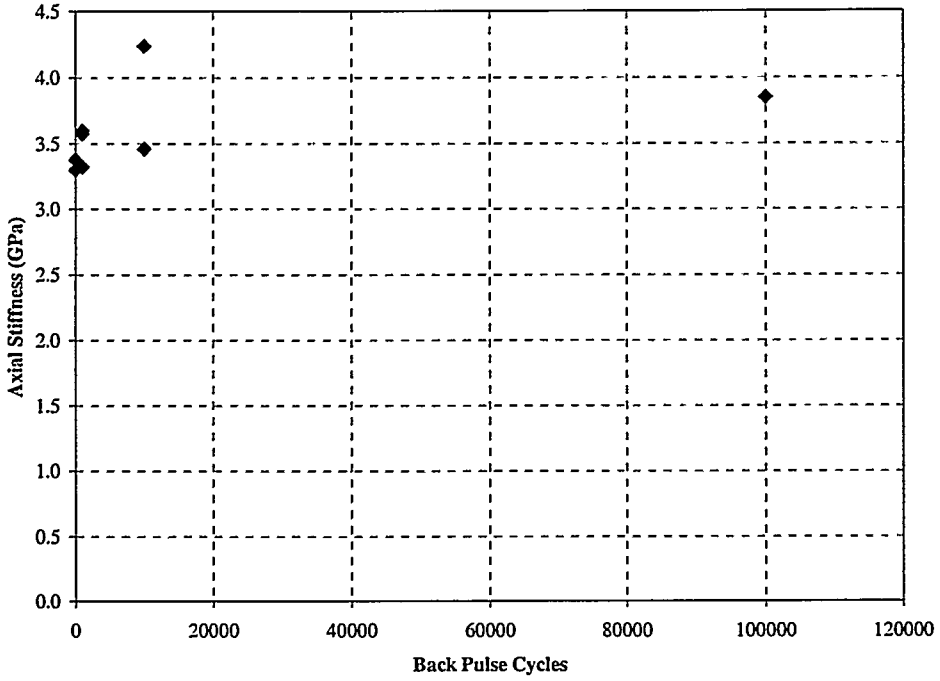

Figure 2: Axial stiffness with exposure to simulated back pulses.

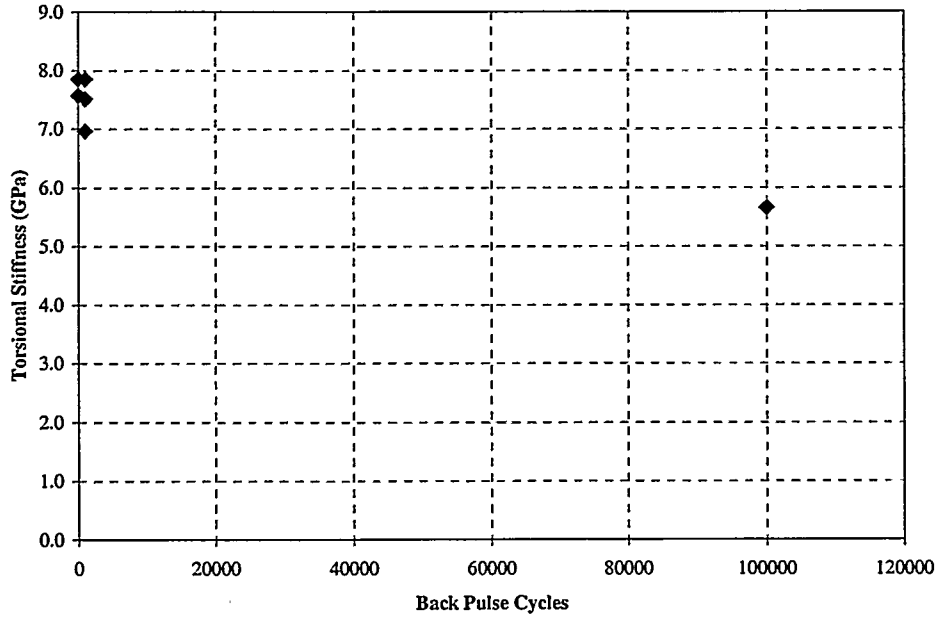

Figure 3: Torsional stiffness with exposure to simulated back pulses.

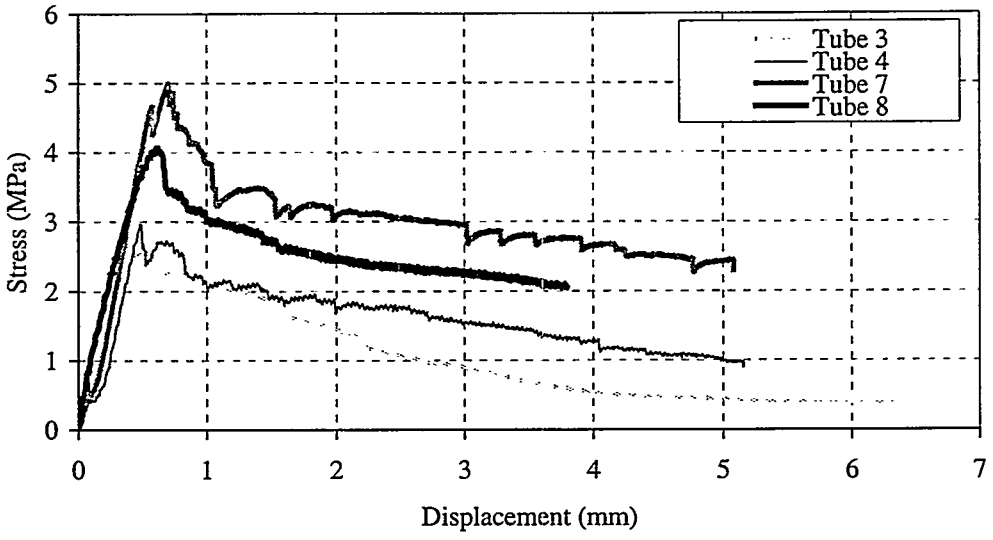

Figure 4: Tensile test results. Tubes 3 and 4 - ceramic end plugs, 7 and 8 – epoxy ends

2.2 Internal pressure tests

The internal pressure test procedure is the same as was described in the paper by Singh, *et al.*[3,4] and is illustrated in Figure 1B. A rubber plug, fabricated slightly smaller than the inner diameter of tube and about the same length, is compressed so that the Poisson expansion provides pressure to the inner surface of the filter section. Test samples ranged from 2.5 to 7.6 cm in length. To prevent frictional loading, two plastic sheets enclosing a lubricant layer were placed at the interface of the plug and filter. During the test, the load and stroke are recorded so that the pressure on the inner surface can be calculated as

$$P_i = \frac{\sigma_p - E_p \varepsilon_z}{2\nu_p} \qquad (1)$$

where P_i is the inner surface pressure, σ_p, E_p, ν_p and ε_z are the applied stress, Young's modulus, Poisson's ratio, and the axial strain of the plug. A plot of the internal pressure vs. axial displacement of the plug is located in Figure 5. The change in the curve at 10 mm is due to the plug making contact with the tube section, and the test program ending at slightly more that 16 mm. The materials did not exhibit catastrophic failure, but underwent a gradual increase in damage throughout the entire sample. There were no preferred failure sites or large crack initiation or propagation. A burst sample at the maximum stroke range is in Figure 6. The surface tows can be seen as they change orientation and pop out of the filter. The matrix material is crumbling and falling off, as can be seen lying around the sample. Once the load is removed, the sample retains its deformed shape and has little structural integrity remaining.

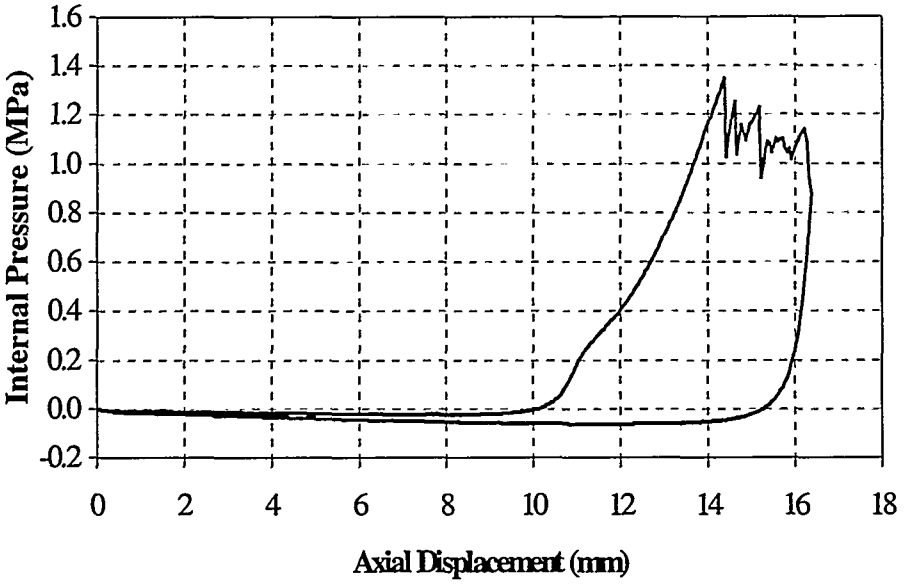

Figure 5: Pressure vs. axial plug displacement curve for internal pressure burst test sample after 10,000 back pulse cycles

The influence of sample size on burst pressure is seen in Figure 7. The data for 25-cm specimens (open square data points) are taken from Alvin, *et al*[3]. This is significant since those tests were performed using a water filled bladder, and should not have effects induced by compressing a rubber plug (frictional loading and non-uniform internal pressure). It should be noted that these results are a combination of as-fabricated and exposed samples. Further testing is needed to produce enough data so that the effects of both thermal cycling and sample length can be separated. The increase in burst pressure with increasing length is believed to be caused by edge effects.

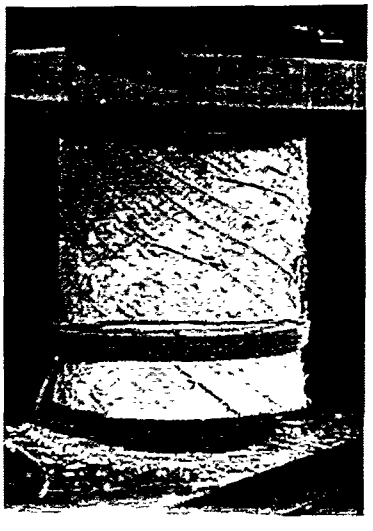

Figure 6: Burst test sample after failure.

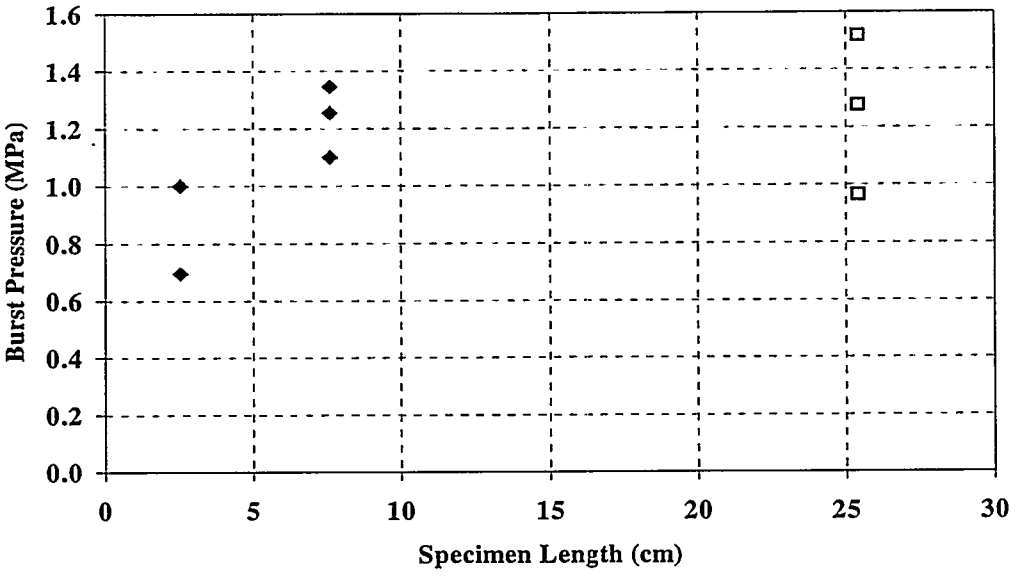

Figure 7: Internal pressure specimen length vs. ultimate burst pressure. (Open square data points taken from Alvin, *et al.*[3])

3. Performance of Nextel/SiC Tubes

In addition to the tests conducted on the hot gas filter materials, mechanical tests have also been conducted on 87% dense Nextel 312/SiC tubes fabricated at ORNL using the FCVI process. The tubes possessed a nominal inner diameter of 50 mm and a nominal wall thickness of 5 mm. Each end of the tube was mounted in epoxy, providing a gage section of approximately 75 mm. Strain rosettes were placed at four equally spaced locations around the circumference to determine all in-plane strain components as well as any bending strains that might be present. An example of such a tube (after failure), illustrating strain gage placement is shown in Figure 8.

Initial characterization focused on determining the mechanical stiffness properties of the tubes. To do so, axial tension and compression tests were conducted to low load levels (well below the matrix cracking stress). Results from such tests are shown in Figure 9. The effective axial stiffness of the tube was found to be 25 msi (171 GPa). Similar tests were conducted in torsion to determine the initial effective shear stiffness of the tube. The results from these tests, shown in Figure 10, exhibit as great deal of scatter.

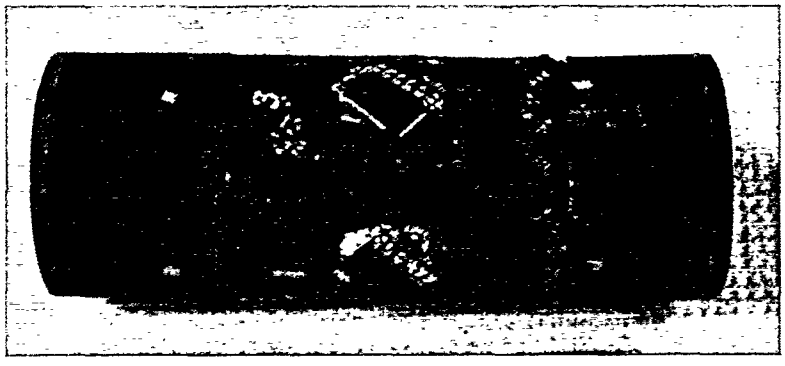

Figure 8: Specimen configuration for dense tube testing.

After the initial mechanical properties had been determined, a quasi-static tensile test was conducted on the first tube section in an attempt to determine the axial strength of the tube. This test resulted in premature failure at the grip region at an applied stress of 30.9 MPa. Subsequent refinement of the gripping procedure for the second tube resulted in behavior that is more representative of the actual performance of the tube. Failure in this case occurred at 68.1 MPa. The results from such tests are summarized in Figure 11. Failure surfaces exhibited significant amounts of fiber pull-out, as illustrated in Figure 12.

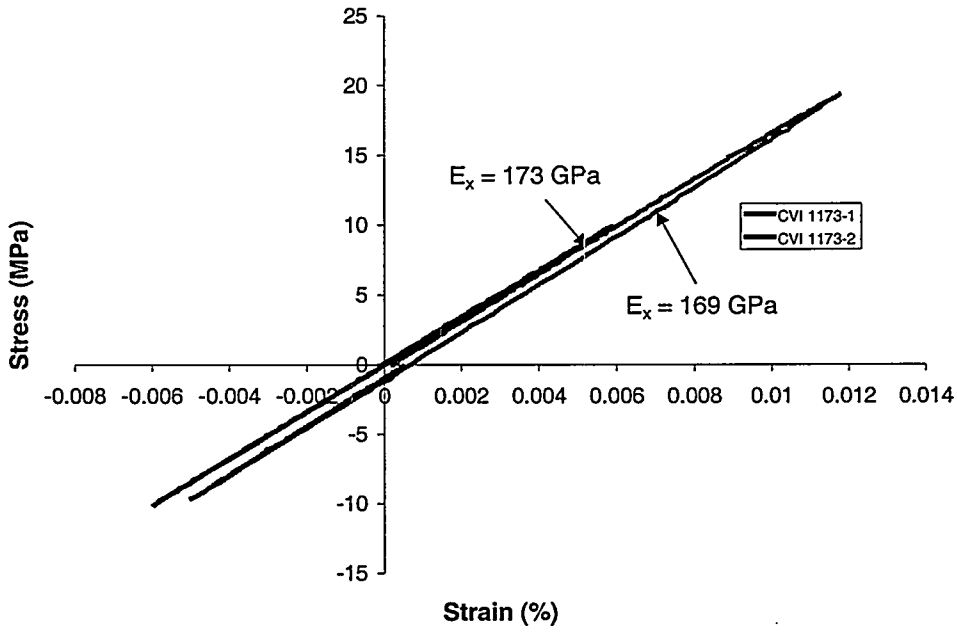

Figure 9: Axial tension and compression test results for Nextel 312/SiC tubes.

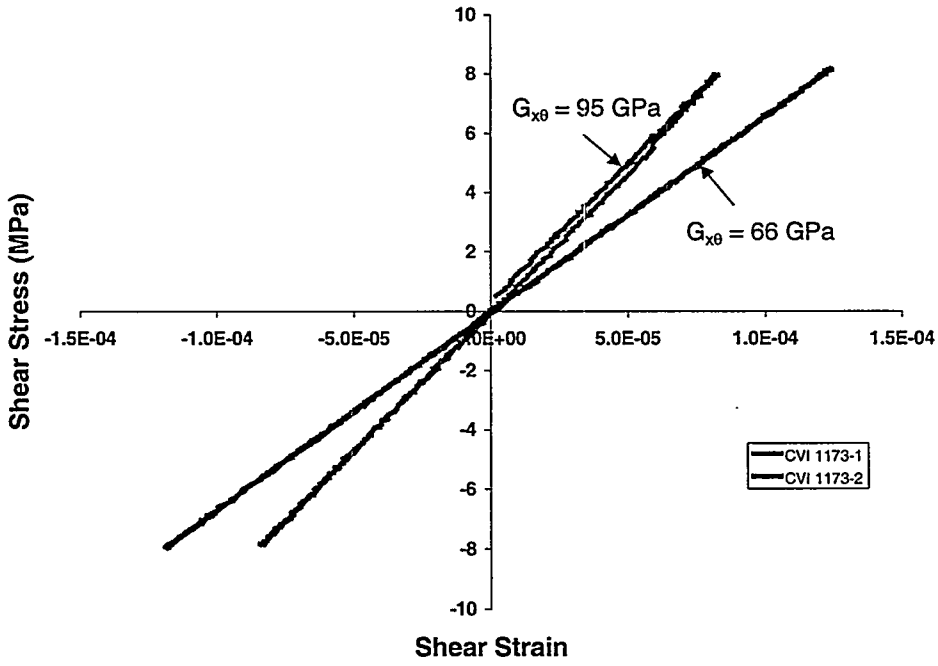

Figure 10: Torsional test results for Nextel 312/SiC tube.

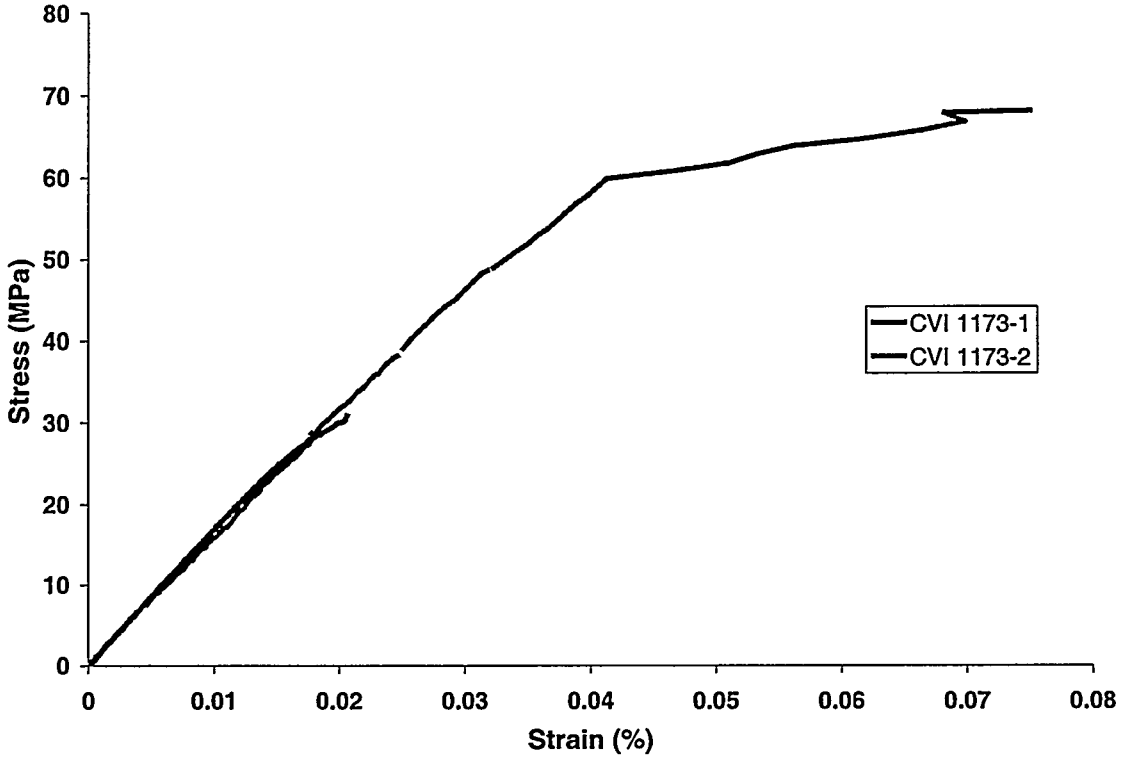

Figure 11: Tensile test results (to failure) for Nextel 312/SiC tubes.

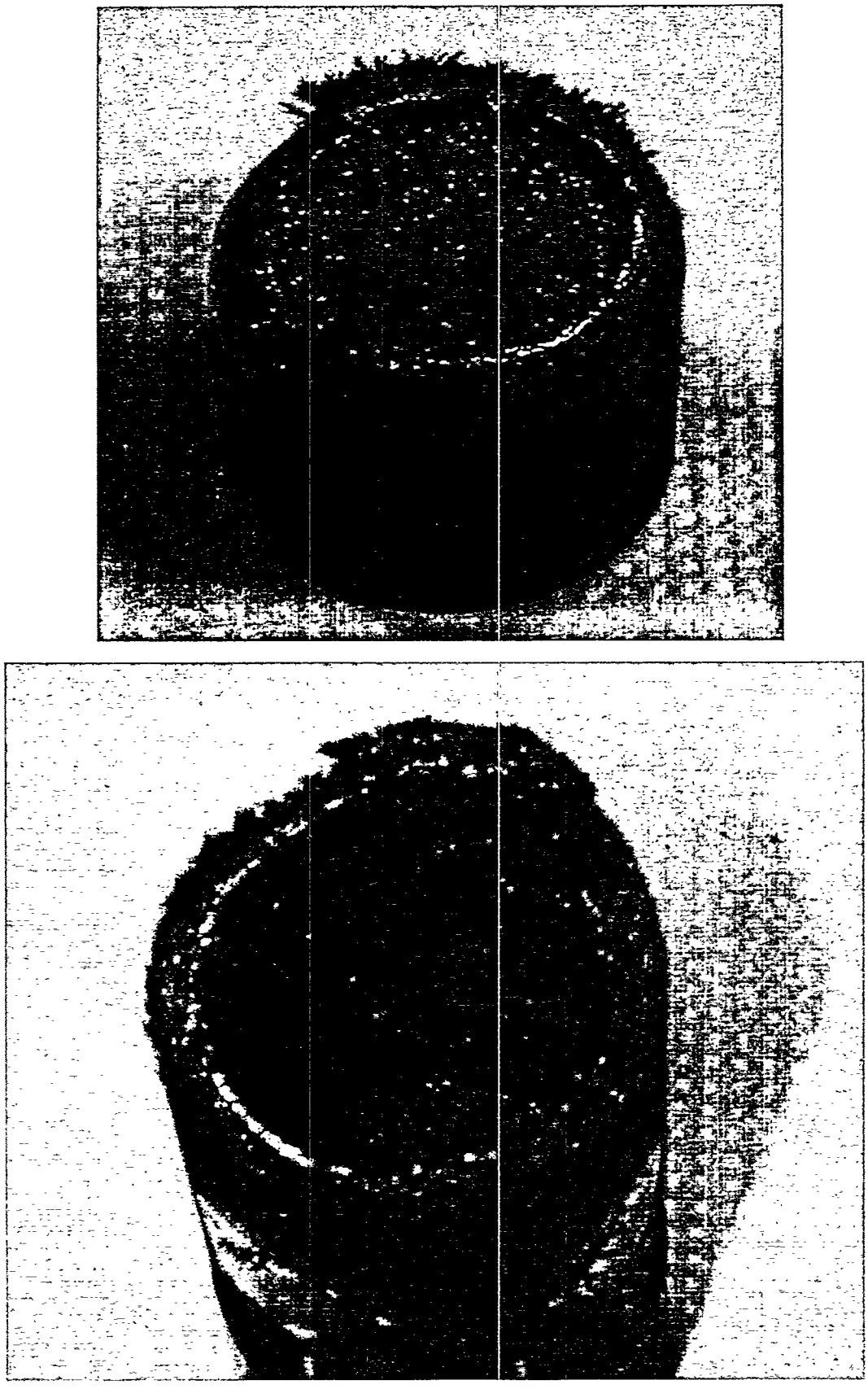

Figure 12: Fracture surfaces of Nextel312/SiC tubes.

4. Crack Bridging Analysis: Aligned Bridging

We have also begun a study of the bridging of short matrix cracks. A schematic of the problem is shown in Figure 13 for two cracks. One crack is fully bridged while the other is partially bridged. This figure shows the relevant parameters of the problem. For a crack of length c, with a bridged length a, we wish to determine the crack shape $u(c)$, the stress intensity factor at the crack tip, and the stress on the bridging fibers.

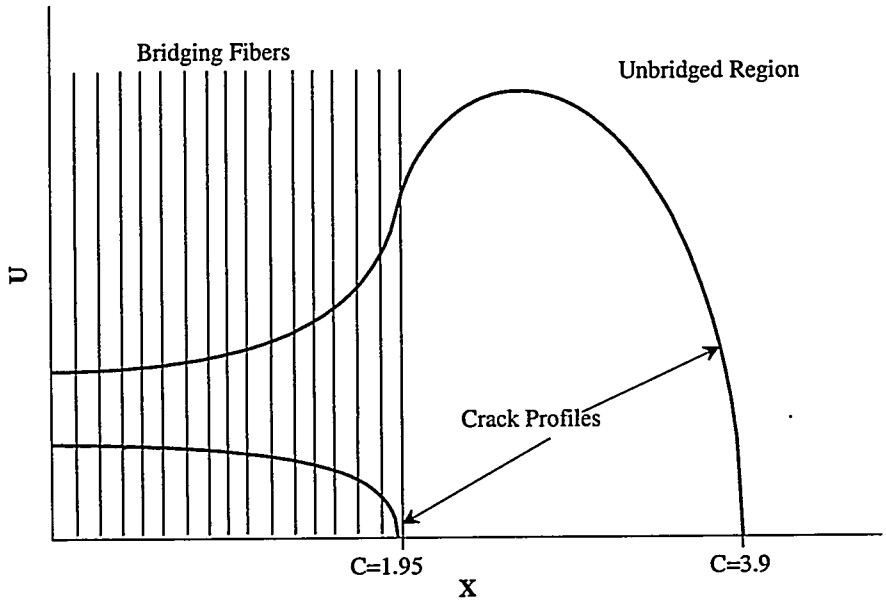

Figure 13: Schematic of centrally bridged crack

This problem is relevant to the issue of bridged matrix cracks at elevated temperatures. As time progresses and the fibers degrade, will the 0° crack extend into the 90° ply or tow?

The equation which we consider gives the equations of shape for a 2-D crack in plane stress with a crack opening displacement $u(x)$ and surface tractions $p(x)$ under uniform remote stress σ_∞. The displacement is related to the traction as follows:

$$u(x)=\frac{2}{\pi^2}\int_x^c \frac{s}{\sqrt{s^2-x^2}}\left\{\int_0^s \frac{\sigma_\infty - p(t)}{\sqrt{s^2-t^2}}dt\right\}ds, 0\le x<c. \qquad (2)$$

Additionally, the stress intensity factor at the crack tip is

$$K=2\sqrt{\frac{c}{\pi}}\int_0^c \frac{\sigma_\infty - p(x)}{\sqrt{c^2-x^2}}dx \qquad (3)$$

Our next task is to determine the bridging law which relates the crack opening to the bridging traction. We have chosen a form given by Danchaivijit and Shetty (DS)[6] which is given by

$$p(u)=\frac{\eta\sigma_\infty}{2(1+\eta)}\left\{\left[1+\frac{16(1+\eta)^2E_f f^2\tau u}{\eta^2\sigma_\infty^2 r}\right]^{\frac{1}{2}}+1\right\} \tag{4}$$

where η is a parameter

$$\eta=\frac{fE_f}{(1-f)E_m} \tag{5}$$

We also normalize the stresses and displacements and substitute the bridging law into the crack shape relationship yielding an integral equation for $U(X)$

$$U(X)=\frac{\gamma C}{S}\int_X^1\frac{s}{\sqrt{s^2-X^2}}\int_0^s\frac{\eta+2-\left[\eta^2+4(1+\eta)U(X)\right]^{1/2}}{\sqrt{s^2-t^2}}dtds \tag{6}$$

where γ, C, U, and S are given by

$$\gamma=\frac{4}{3(1+\eta)}$$

$$C=\frac{c}{c_0};\ c_0=\pi\left(\frac{K_{cm}}{\alpha}\right)^{\frac{2}{3}}(1-f)^2(1+\eta)^2$$

$$U=\frac{u(x)}{u_0};\quad u_0=\frac{\sigma_\infty^2 r}{4(1+\eta)E_f f^2\tau} \tag{7}$$

$$S=\frac{\sigma_\infty}{\sigma_0};\quad \sigma_0=\left(\alpha K_{cm}^2\right)^{1/3},\ \alpha=\frac{6(1-\nu^2)\tau E_f f^2(1-f)(1+\eta)^2}{rE_m}$$

Note that σ_0 is the Aveston, Cooper, and Kelly (ACK) matrix cracking stress[7].

Finally, the order of integration is reversed which yields improved convergence properties

$$U(X)=\frac{4C}{3S(1+\eta)}\left[\int_0^X\left[2+2\eta+P(X)\right]\ln\left|\frac{\sqrt{1-t^2}+\sqrt{1^2-X^2}}{\sqrt{t^2-X^2}}\right|dt+\int_X^1\left[2+2\eta+P(X)\right]\ln\left|\frac{\sqrt{1-t^2}+\sqrt{1^2-X^2}}{\sqrt{X^2-t^2}}\right|dt\right]$$

$$P(X)=\left[\eta^2+4(1+\eta)U(x)\right]^{\frac{1}{2}}-\eta \tag{8}$$

The resulting equation is then iterated until convergence in $U(X)$ is obtained. If the critical stress required for crack extension is desired, the crack-tip stress intensity factor can then be found and compared to the critical stress intensity factor. If the condition is

not met, the applied stress, S, can be altered and the crack shape iterated again. This process continues until both the shape and the stress intensity factor conditions are met. For a more complete treatment of this problem, the reader is referred to Danchaivijit and Shetty[5].

For a partially bridged crack, the bridging law $P(X)$ is set to zero over some portion of the crack. As an example of the technique, we compare the results obtained from using the DS bridging expression to the results from an earlier expression from Marshall, Cox, and Evans (MCE)[8], namely

$$p(u) = \left[\frac{4\tau f^2 E_f (1+\eta)}{r}\right]^{\frac{1}{2}} u^{\frac{1}{2}} \qquad (9)$$

For unidirectional dense alumina fiber/alumina-yttria matrix composites at room temperature, η is found experimentally to be 3.56. The normalizing stress, σ_0, is the ACK cracking stress, 458 MPa. The normalizing crack length, c_0, is 1.01 mm. Given the fiber volume fraction of 48.5% and the fiber radius of 6μ, we find that the normalizing crack length covers approximately 40 fibers.

Figure 14 shows the effect of the two bridging laws on the calculated matrix cracking stress of the unidirectional oxide/oxide materials. For long cracks, the two expressions yield nearly identical matrix cracking stresses, but for short to intermediate cracks, the DS expression results in higher stresses.

The extension of 0° tow cracks into the 90° tow will be affected by the properties of the 90° tow. For example, the stress carried by the 90° tow will be dependent on its modulus, and crack extension will be governed by its fracture toughness. As an example, we can consider a crack which extends from the 0° tow into the 90° tow. The crack is 'half-bridged' with equal regions in the 0° tow and in the 90° tow. The stress ratio is defined as the far-field stress (σ_∞) carried by the 90° region compared to the 0° stress.

We shall assume that the fracture toughness of the two regions is identical. The resulting plot for various total crack sizes, C, is shown in Figure 15, which demonstrates that as the stress carried by the unbridged region decreases, a greater far field stress is required for crack extension. In general, the critical stress for crack extension depends on the initial crack length, the bridging extent, and the stress ratio.

Our other interest is in the stress carried by the centrally bridged fibers, as this will govern their strength degradation. Figure 16 shows the stress carried by the fibers for a crack in the 0° tow of a Hi-Nicalon/CVI Silicon Carbide composite that we have tested recently[9]. The relevant mechanical properties are

$E_f = 270\text{GPa}$ $\qquad$ $\sigma_0 = 290\text{MPa}$

$E_m = 310 GPa$ $\qquad$ $c_0 = 78\mu$

$f = 0.342$ $\qquad$ $\eta = 0.452$

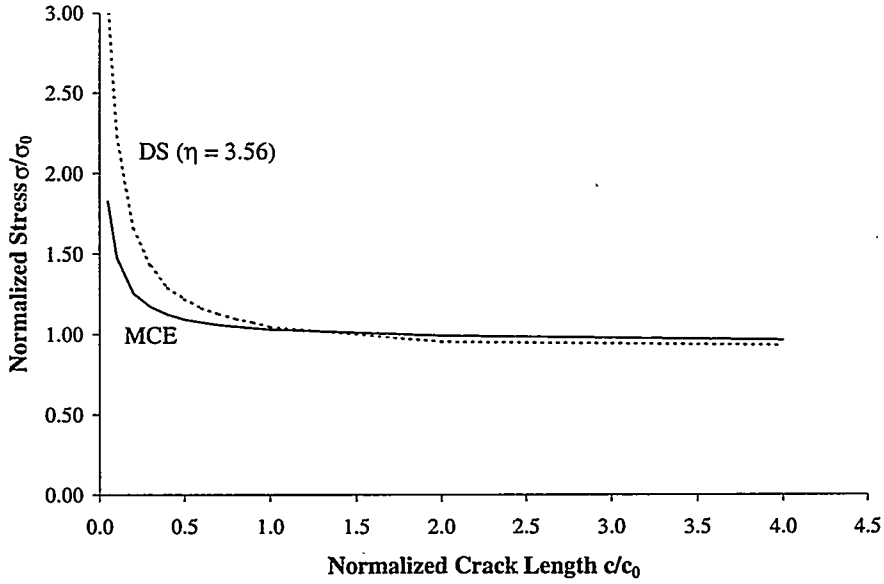

Figure 14: Effect of MCE and DS bridging laws on matrix cracking of unidirectional materials

The geometry of the tow revealed a thickness of 152 μ, approximately twice the length required for a steady-state matrix crack. Here we consider a matrix crack which crosses the entire 0° tow (*C=1.95*) and cracks which grow progressively into the 90° tow, ending with a crack which extends through the 0° tow and halfway into the adjacent 90° tow (*C=3.90*). The appropriate stress ratio is unity, and the applied stress is arbitrarily set to 80 MPa. As the crack extends into the 90° tow the stress carried by the intact fibers increases, especially near the 0°/90° tow interface. For the largest crack, the stress at the interface is greater than the steady-state fiber stress. Ultimately, for the long crack the average fiber stress should approach unity.

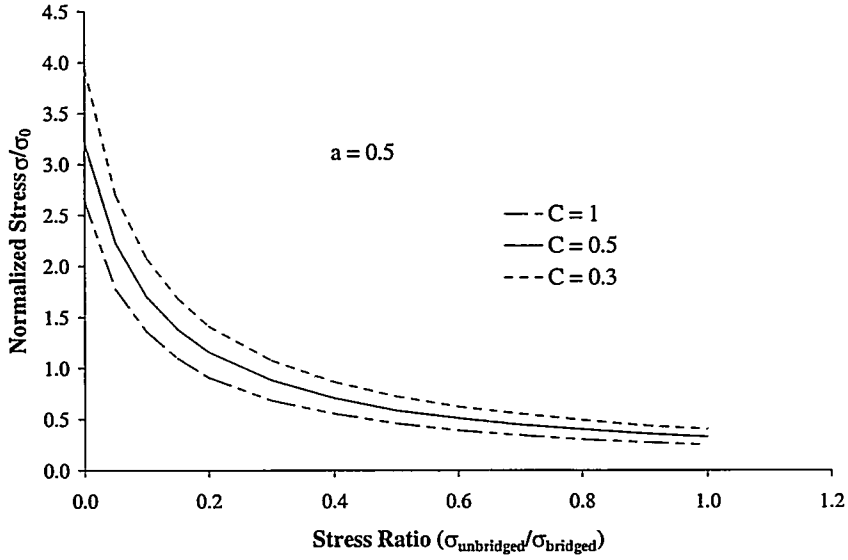

Figure 15: Effect of stress ratio on critical matrix cracking stress

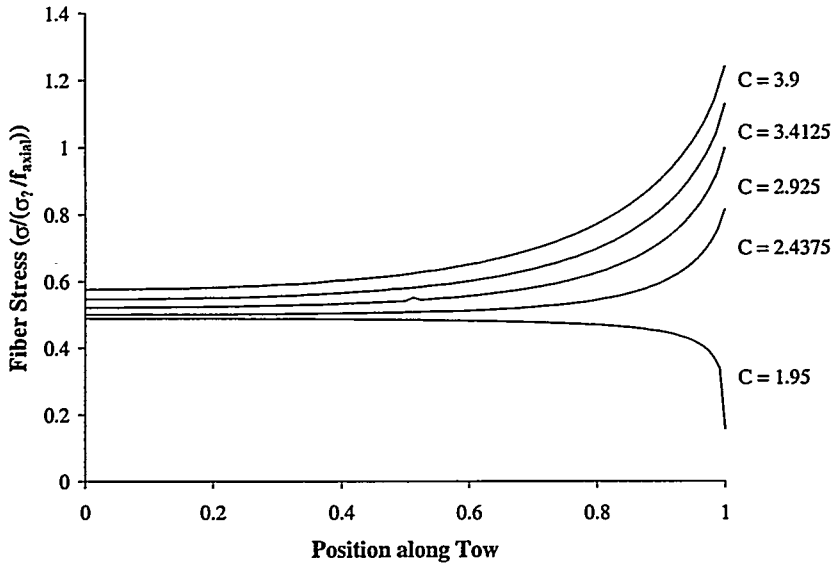

Figure 16: Stress carried by central fibers for a partially bridged crack

5. Crack Bridging Analysis: Randomly Distributed Fibers

5.1 Crack Closure Pressure for an Inclined Fiber

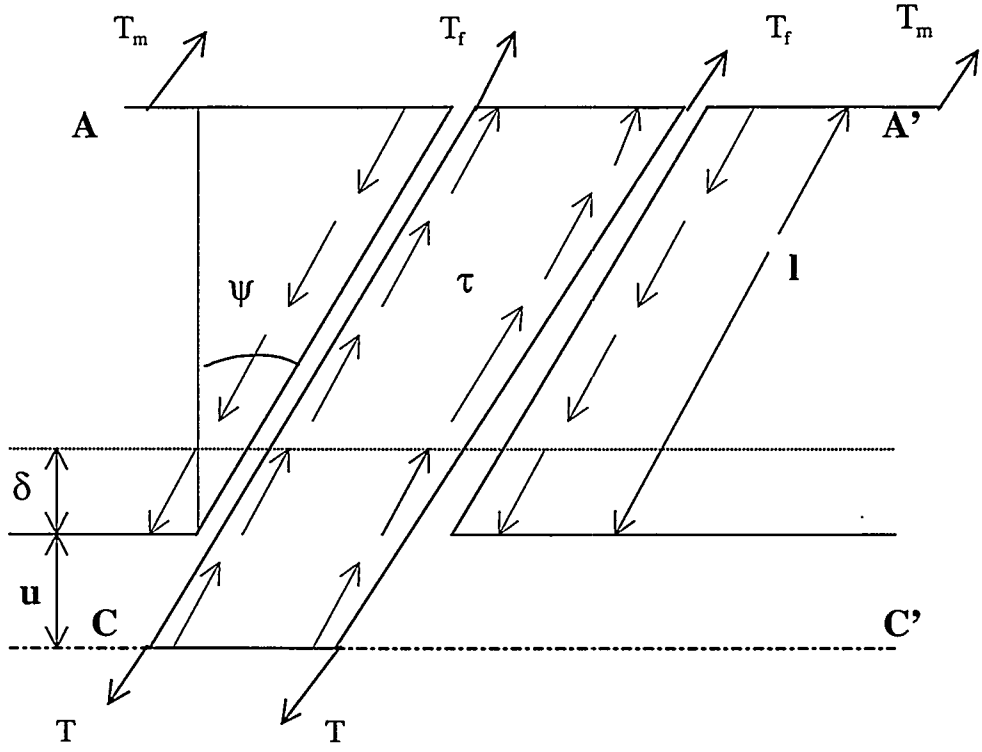

Figure 17: Analysis of fiber pullout for an inclined fiber.

The mechanics of fiber pullout can be conveniently analyzed by applying tractions T_m and T_f equal and opposite to the stresses in the matrix and fibers along AA' at the end of the slipped region, and removing the section AA'CC'. If we neglect the effect of shear stresses above AA' (i.e., assume that it represents an isostrain plan) these tractions are related:

$$\frac{T_m}{E_m} = \frac{T_f}{E_f} \tag{10}$$

where

T_m and T_f are the tractions within the matrix and the fiber respectively;
E_m and E_f are the modulus within the matrix and the fiber respectively.

Equations relating the stresses and displacements are obtained by considering the equilibrium of the matrix and fiber separately and also calculating the extensions δ and δ+u of the matrix and fiber.[8]

Matrix equilibrium: $$T_m A_m \cos\psi = 2\pi R\tau l \cos\psi \quad (11)$$

Fiber equilibrium: $$TA_f \cos\psi = T_f A_f \cos\psi + 2\pi R\tau l \cos\psi \quad (12)$$

Matrix elongation: $$\frac{\delta}{l\cos\psi} = \frac{\pi R l \tau}{A_m E_m} \quad (13)$$

Fiber elongation: $$\frac{\delta}{l\cos\psi} + \frac{u}{l\cos\psi} = \frac{T_f}{E_f} + \frac{\pi R l \tau}{A_f E_f} \quad (14)$$

where

ψ = fiber angle
A_m = area of matrix per fiber
A_f = fiber cross-sectional $A_f = \pi R^2$
R = fiber radius
l = sliding length
τ = shear stress
δ = elongation
u = crack opening

From Equations (10) and (11), we have

$$T_f = \frac{2\pi R l \tau}{A_m}\frac{E_f}{E_m} \quad (15)$$

From Equations (12) and (15), we have

$$T = \frac{2l\tau}{R}[1+\eta] \quad (16)$$

with

$$\eta = \frac{E_f A_f}{E_m A_m} = \frac{E_f V_f}{E_m V_m} \quad (17)$$

If we substitute Equations (13) and (15) into Equation (14), we find:

$$\frac{u}{l} = \frac{2\pi R l \tau \cos\psi}{A_m E_m} + \frac{\pi R l \tau \cos\psi}{A_f E_f} - \frac{\pi R l \tau \cos\psi}{A_m E_m} \quad (18)$$

After some simplification, we can find the sliding length l:

$$l^2 = \frac{uRE_f}{\tau(1+\eta)\cos\psi} \quad (19)$$

Finally, by combining Equations (16) and (19), we obtain the traction T:

$$T = \left[\frac{4uE_f\tau(1+\eta)}{R\cos\psi}\right]^{1/2} \quad (20)$$

5.2 *Extension to Randomly Distributed Fibers*

We now seek to extend the solution for the closure traction to the analysis of cracks that are bridged by randomly oriented fibers. These fibers are assumed to be sufficiently long that pull-out does not occur. For such a case, the probability density function describing the orientation of fibers in the matrix is defined as (with the normalization condition)

$$F(\psi) = \int_0^{\psi} f(\psi) d\psi$$
$$F\left(\frac{\pi}{2}\right) = 1 \tag{21}$$

If we consider $f(\psi) =$ constant (so that the distribution is completely random), we find that

$$f(\psi) = \frac{2}{\pi} \tag{22}$$

Following Jain and Wetherhold[10], we introduce the auxiliary variable y', which represents the signed distance from fibers' center to the crack plane. The required probability density is:

$$P[E_1 E_2] \tag{23}$$

where,

$$E_1 = y' \in [y', y' + dy']$$
$$E_2 = \psi \in [\psi, \psi + d\psi] \tag{24}$$

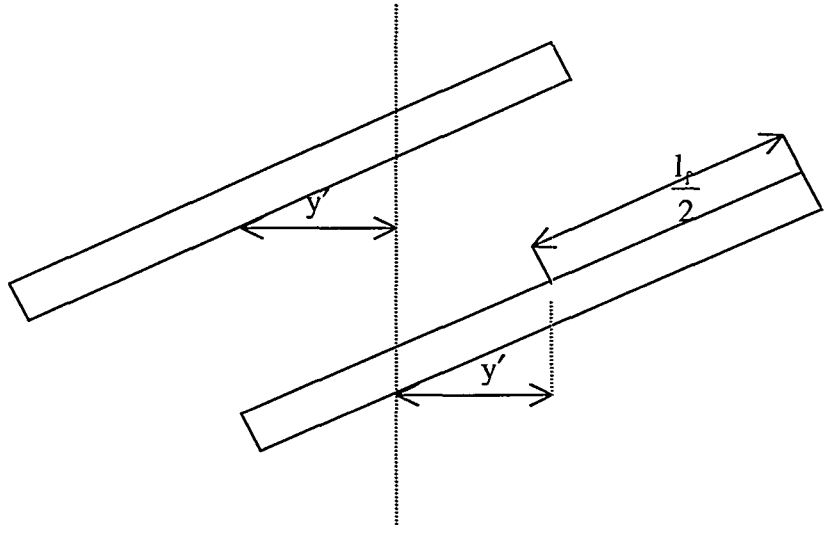

Figure 18: Illustration of the definition of the auxiliary variable y'.

Using the Bayes' theorem for non-independent events E_1 and E_2 we can write:

$$P[E_1 E_2'] = P\left[E_1 / E_2\right] \bullet P[E_2] \tag{25}$$

The second probability is well defined by Equation (22). For the events E_1 the only values of y' are those which intercept the crack, i.e. $y' \in \left[\frac{-l_f}{2}\cos\psi, \frac{l_f}{2}\cos\psi\right]$. Under the assumption that the fiber center of gravity is uniformly distributed in y direction $\left[f_y(y) = \frac{1}{h}, y \in [0, h]\right]$, we can say that y' is also uniformly distributed $\left[f_{y'}(y) = \frac{1}{h}, y' \in [\Pi - h, \Pi]\right]$. We may study $y' \in \left[0, \frac{l_f}{2}\cos\psi\right]$ and multiply that probability by 2.

The probability density that a single fiber bridges an arbitrary crack plane $y = \Pi$ with events E_1 and E_2 is thus:

$$\begin{cases} dN_f = \left(\frac{2}{\pi}\right)\left(\frac{2}{h}\right) d\psi\, dy' \\ \quad = 0 \ \ elsewhere \end{cases} \tag{26}$$

The number of fibers crossing the crack plane with events E_1 and E_2 is defined as:

$$N_{fc} = \left(\frac{2}{\pi}\right)\left(\frac{2}{h}\right) N_f \int_0^{\frac{\pi}{2}} \int_0^{\frac{l_f}{2}\cos\psi} dy' d\psi \tag{27}$$

where,

h – width of the composite plate
N_f – total number of fiber in the sample.

$$N_f = \frac{A_c h V_f}{A_f l_f} \tag{28}$$

The closure pressure is defined as:

$$P(y) = T(y) V_{fc} \cos^2\psi \tag{29}$$

where,

$$V_{fc} = \frac{A_f l_f}{A_c h} N_{fc} \tag{30}$$

is the volume fraction of the fibers that bridge the crack plane Π with events E_1 and E_2. By taking into account Equation (27)and Equation (28) we can write:

$$V_{fc} = \left(\frac{2}{\pi}\frac{2}{h}\int_0^{\frac{\pi}{2}} \int_0^{\frac{l_f}{2}\cos\psi} d\,y' d\psi\right) V_f \tag{31}$$

Thus, if the crack is large enough that that bridging fibers are randomly distributed, the approximate closure pressure as a function of position is given by

$$P(y)=\left(\frac{2}{\pi}\right)\left(\frac{2}{h}\right)V_f\int_0^{\frac{\pi}{2}}\int_0^{\frac{l_f}{2}\cos\psi}\left[\frac{4u(y)E_f\tau(1+\eta)}{R\cos\psi}\right]^{1/2}\cos^2\psi\,dy'd\psi \tag{32}$$

After integration we have

$$P(y)=\left(\frac{2}{\pi}\right)\left(\frac{l_f}{h}\right)\left[\frac{4u(y)E_f\tau(1+\eta)}{R}\right]^{1/2}V_f\int_0^{\frac{\pi}{2}}\left(\sqrt{\cos\psi}\right)^5 d\psi \tag{33}$$

If we evaluate the integrand numerically, we obtain the final result that

$$P(y)\approx 0.457\left(\frac{l_f}{h}\right)\left[\frac{4u(y)E_f\tau(1+\eta)}{R}\right]^{1/2}V_f \tag{34}$$

so that for the case in which the length of the fibers is the same as the length of the composite, the average bridging stress is roughly half that which would be expected if the fibers were aligned with the loading direction.

Once the average crack closure traction is obtained, it is possible to determine the crack shape in the manner described in the previous section. The resulting crack shape may then be used to determine the stress intensity factor at the crack tip as a function of the global applied load.

6. Life Prediction Analysis for Multiple Damage Mechanisms

The last aspect of our work to be described in this report is on the life prediction of ceramic composite materials that experience combined degradation mechanisms. In previous reports, we have described two different techniques for accomplishing this task: (1) micromechanical models that combine the two mechanisms through either analytical results or simulation results[9], and (2) residual strength based approach (MRLife or CCLife)[9, 11]. The first approach tends to be more computationally intensive limiting its applicability to real composite structures, while the second approach often requires extensive experimental characterization and phenomenological representations of the resulting data. In this effort, we seek to merge the two approaches by using the results of the detailed micromechanical simulations for two individual degradation mechanisms as input to the residual strength approach. The residual strength approach is then used to predict the combined behavior.

The first damage mechanism to be considered is that of slow crack growth in the fibers. The analysis of this damage mechanism has been described in detail in a previous report, and will not be repeated here.

The second mechanism to be considered is asperity creep along the interface. For this mechanism acting alone, we use a simple model with a few main assumptions

- The fibers creep while the matrix, which carries no load, does not
- The fiber creep reduces the asperity amplitude only – not the fiber radius
- The composite strength is governed by the tensile strength equation – no fiber degradation

We begin the analysis with the relationship between asperity height and frictional stress, where A is a combination of elastic constants

$$\tau = A\frac{h}{r} \tag{35}$$

Next, we assume that fiber creep changes the asperity height, h, only, and use a power law creep rate $\dot{\varepsilon} = B\sigma^n$ to obtain the frictional stress, τ, as a function of time

$$\tau = \frac{A}{r}\left[h_0 - \frac{1}{2}B\sigma^n t(r+h_0)\right] \tag{36}$$

In deriving Equation (36), we have assumed that the volume of the fiber remains constant during the creep process.

Now that we have the frictional stress as a function of time, we may substitute Equation (36) into the Curtin tensile strength expression

$$\sigma_u = f\left(\frac{\sigma_0^m l_0 \tau}{r}\right)^{\frac{1}{m+1}}\left(\frac{2}{m+2}\right)^{\frac{1}{m+1}}\left(\frac{m+1}{m+2}\right) \tag{37}$$

to obtain a normalized composite strength

$$\frac{\sigma_u}{\sigma_{u0}} = \left[1 - \frac{1}{2} B\sigma^n t\left(1 + \frac{r}{h_0}\right)\right]^{\frac{1}{m+1}} \tag{38}$$

with a failure time

$$t = \frac{2}{\left(1 + \frac{r}{h_0}\right) B\sigma^n}\left[1 - \left(\frac{\sigma}{\sigma_{u0}}\right)^{m+1}\right] \tag{39}$$

Figure 19 shows a plot of this failure time along with failure times determined by numerical simulation with initial asperity height 100μm. The agreement between simulation and analysis is fairly good. Increasing the composite length makes only a slight difference in simulated lifetimes, unless the applied stress is very near the bundle strength of the material. Results are also shown for the analysis with a 20μm asperity height.

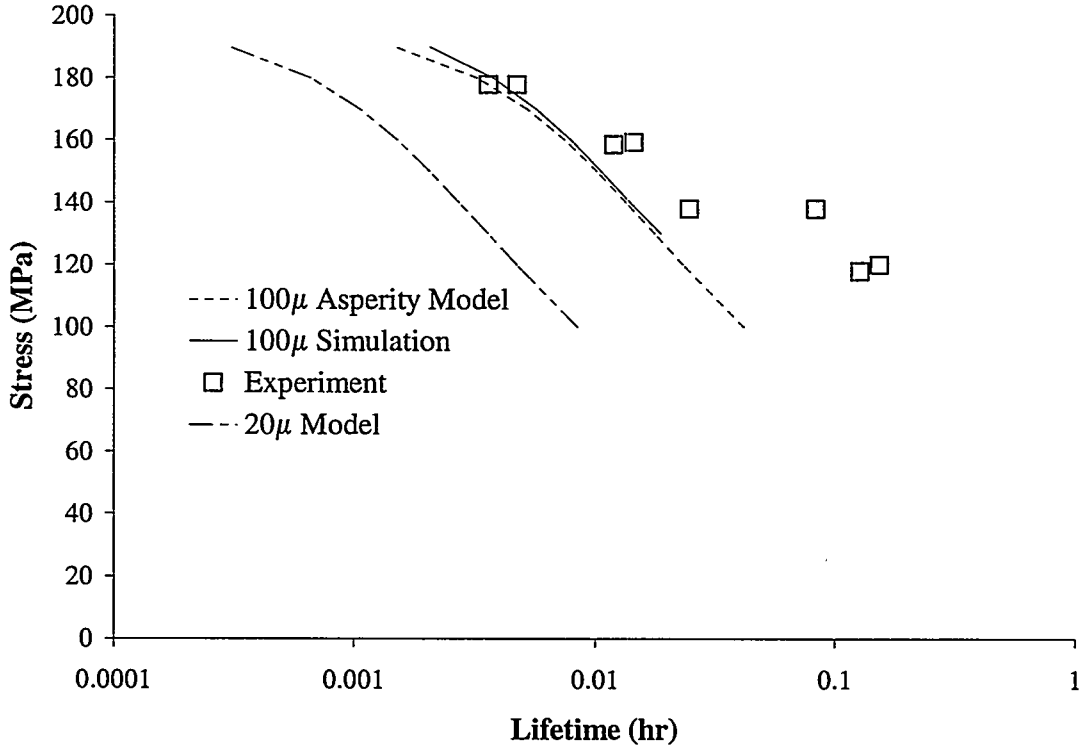

Figure 19: Asperity analysis for woven composites containing Nextel 610 fibers with an alumina-yttria matrix.

We now seek to combine the effects of the two mechanisms. As input to the slow crack growth model, we may use the single fiber data from Yun and DiCarlo[12] for Nextel 610 fibers. We are less certain about the asperity creep. However, for the purposes of demonstrating the manner in which the two mechanisms may be combined, we assume an

asperity creep behavior that gives us the same composite time to failure at an applied stress level of 170 MPa as does the slow crack growth model. This situation (that in which the mechanisms act on the same time scale) should give us the greatest interaction between the two mechanisms.

For the residual strength approach, a number of different models have been suggested. For simplicity, in this work we employ the wear-out model so that the rate of change of the normalized remaining strength, *Fr*, for a single damage mechanism is given in terms of the normalized applied stress, *Fa*, by

$$\frac{dFr}{dt} = -\frac{f}{\alpha} Fa^{\alpha} Fr^{1-\alpha} \tag{40}$$

where f and α are constants that depend upon the value of *Fa*. If we integrate Equation (40) for the case in which *Fa* is constant with respect to time, and simplify, we obtain

$$Fr = \left[1 - \left(1 - Fa^{\alpha}\right)\frac{t}{t_f}\right]^{\frac{1}{\alpha}} \tag{41}$$

where t_f is the time to failure.

For the combined mechanism case, we assume that the rate of change of remaining strength may be given by

$$\frac{dFr}{dt} = -\frac{1}{\alpha_1 t_{f1}}\left(1 - Fa^{\alpha_1}\right)Fr^{1-\alpha_1} - \frac{1}{\alpha_2 t_{f2}}\left(1 - Fa^{\alpha_2}\right)Fr^{1-\alpha_2} \tag{42}$$

where α_1 and t_{f1} correspond to the first mechanism (slow crack growth), and α_2 and t_{f2} correspond to the first mechanism (asperity creep).

To compare the two analysis results, we proceed as follows. First, we perform the simulations for the slow crack growth and asperity creep mechanisms acting independently. The results from the simulations for each mechanism are fit to Equation (41) using a least squares method to determine α_1, t_{f1}, α_2, and t_{f2}. Then Equation (42) is evaluated numerically to predict the combined behavior. The predicted combined behavior is then compared to the simulation results. Results of such a comparison are shown in Figure 20 for the 170 MPa applied load. We see that the residual strength approach accurately predicts the simulation results for this case. This process has been repeated at different applied stress levels with similar success[13]. The importance this result is the implication for the analysis of real composite structures. In such structures, the simulation approach is (presently) too computationally intense to be applied directly. However, the results from the simulation may be used as inputs to the less computationally intense residual strength approach, which may then be applied to the structural analysis.

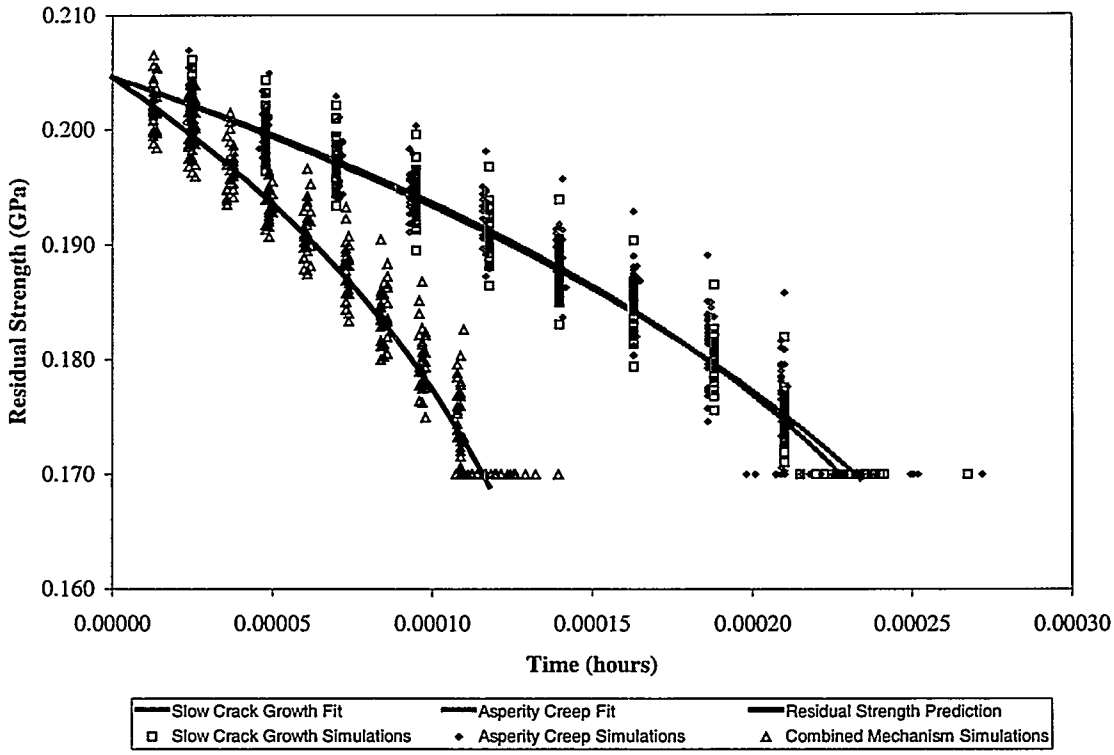

Figure 20: Comparison of simulation results and residual strength results.

7. Summary

This report describes the results from the research program of the Materials Response Group at Virginia Tech addressing the need for reliable and durable ceramic composites to perform in high temperature applications. Included in this effort is the mechanical property characterization of oxide/oxide hot gas candle filters under tensile loads and internal pressure. In addition, the mechanical properties of dense Nextel/SiC structural tubes have been determined by applying axial tensile and compression loading as well as to torsional loading.

In conjunction with these experimental characterizations of composite performance, we have also described a number of modeling activities that are of importance for relating the behavior of the composite to the behavior of the constituents. The first of these modeling activities is the development of an understanding of the bridging stresses in cracks that extend into both 0° and 90° plies. The stress concentrations that result in the 0° plies may be important for making accurate predictions of the tensile strength of cross-plied and woven laminates. Also, we have described our efforts toward achieving the goal of developing models for the strength and toughness of fibril-reinforced composites, beginning with the development of a model for the bridging stresses in cases in which the bridging fibers are randomly oriented.

In the last modeling effort described we were successful in joining two types of durability models that include the effects of multiple degradation mechanisms: those based upon detailed micromechanical simulations of the composite behavior and those based upon remaining strength. To do so, we used the results from the micromechanical simulations for single degradation mechanisms acting independently as inputs to the remaining strength model. The remaining strength model was then used to predict the combined behavior. The comparison with the simulation result was seen to be very good.

8. References

[1] P.G. LeHaye and M.R. Bary, Externally fiber combustion cycle (EFCC) A DOE Clean Coal Project: Effective means of rejuvenation for older coal-fired stations, Int. Gas Turbine and Aeroengine Congress and Exposition, Paper #94-GT-483, ASME (New York, 1994)

[2] R. R. Judkins, et al., Development of ceramic composite hot-gas filters, Int. Gas Turbine and Aeroengine Congress and Exposition, Paper # 95-GT-305, ASME (1995).

[3] X. Huang, R. H. Carter, and K. L. Reifsnider, "Experimental Study and Modeling of a Novel Ceramic Composite Hot Gas Candle Filter Material," *Ceramic Engineering and Science Proceedings*, **19** [3], (1998).

[4] M. A. Alvin, T. E. Lippert, E. E. Smeltzer, and G. J. Bruck, "Advanced Hot Gas Filter Performance and Characterization," Presented at the Advanced Coal-Based Power and Environmental Systems Conference, Morgantown, WV, July 21-23, (1998).

[5] J. P. Singh, M. Sutaria, and W. Bielke, "Thermal Shock Behavior of Advanced Ceramic/Composite Hot-Gas Filters" *Ceramic Engineering and Science Proceedings*, **18**[3], pp.719-727, (1997).

[6] S. Danchaivijit and D. K. Shetty, "Matrix Cracking in Ceramic-Matrix Composites", *J. Amer. Cer. Soc.*, Vol. 76, pp. 2497-2504, (1993).

[7] J. Aveston, G. A. Cooper, A. Kelly, "Single and Multiple Fracture" The Properties of Fibre Composites, Conference Proceedings, National Physical Laboratory, Guilford, U.K., pp. 15-26, (1971).

[8] D. B. Marshall, B. N. Cox, A. G. Evans, "The Mechanics of Matrix Cracking in Brittle-Matrix Fiber Composites", *Acta. Metall*, Vol. 33, pp. 2013-2021 (1985).

[9] W. A. Curtin, H. Halverson, R. H. Carter, N. Miraj, and K. L. Reifsnider, "Investigation of Properties and Performance of Ceramic Composite Components: Final Report on Phases III and IV," ORNL/sub/87-SA946/06, report prepared for ORNL under subcontract number 19X-SA496C, January 1998.

[10] L.K. Jain, R.C. Wetherhold, "The Effect of Fiber Orientation on the Fracture Toughness of Brittle Matrix Composites", *Acta. Metall. Mater*, **40** [6], pp. 1135-1143 (1992).

[11] K. L. Reifsnider, W. W. Stinchcomb, L. Oleksuk, S. S. Lee, "Effect of Elevated Temperature and Cyclic Loading on Properties and Damage Modes in Ceramic

Composites," ORNL/sub/87-SA946/03, report prepared for ORNL under subcontract number 19X-SA496C, November 1993.

[12] H. M. Yun, and J. A. DiCarlo, "Time/Temperature Dependent Tensile Strength of SiC and Al_2O_3-Based Fibers", *Advances in Ceramic Matrix Composites III*, Ceramic Transactions, Vol. 74, pp. 17-25 (1996).

[13] S. W. Case and H. G. Halverson, "Residual Strength Based Life Prediction of Composite Materials," to be submitted to *Journal of Composites Technology and Research*, July 1999.

CERAMIC COMPOSITES DISTRIBUTION

3M COMPANY
Ceramic Materials Department
201-4N-01 3M Center,
St. Paul, MN 55144
M. A. Leitheiser

AIR PRODUCTS AND CHEMICALS
P.O. Box 538
Allentown, PA 18105
S. W. Dean

ALBANY RESEARCH CENTER
1450 Queen Avenue, SW
Albany, OR 97321
R. P. Walters

ALLISON GAS TURBINE DIVISION
P.O. Box 420
Indianapolis, IN 46206-0420
P. Khandelwal (Speed Code W-5)
R. A. Wenglarz (Speed Code W-16)

AMA RESEARCH & DEVELOPMENT CENTER
5950 McIntyre Street
Golden, CO 80403
T. B. Cox

ARGONNE NATIONAL LABORATORY
9700 S. Cass Avenue
Argonne, IL 60439
W. A. Ellingson
J. P. Singh

BABCOCK & WILCOX
Domestic Fossil Operations
20 South Van Buren Avenue
Barberton, OH 44023
M. Gold

BOSTON UNIVERSITY
Manufacturing Engineering
44 Cummington Street
Boston, MA 02215
V. Sarin

BRITISH COAL CORPORATION
Coal Technology Development Division
Stoke Orchard, Cheltenham
Glocestershire, England GL52 4ZG
J. Oakey

DOE
DOE OAK RIDGE OPERATIONS
P. O. Box 2008
Building 4500N, MS 6269
Oak Ridge, TN 37831
M. H. Rawlins

DOE
OFFICE OF BASIC ENERGY SCIENCES
Materials Sciences Division
ER-131
19901 Germantown Road
Germantown, MD 20874-1290
H. M. Kerch

DOE
FEDERAL ENERGY TECHNOLOGY CENTER
3610 Collins Ferry Road
P.O. Box 880
Morgantown, WV 26507-0880
R. C. Bedick
D. C. Cicero
F. W. Crouse, Jr.
R. A. Dennis
N. T. Holcombe
W. J. Huber
T. J. McMahon
J. E. Notestein

DOE
FEDERAL ENERGY TECHNOLOGY CENTER
626 Cochrans Mill Road
P.O. Box 10940
Pittsburgh, PA 15236-0940
A. L. Baldwin
G. V. McGurl
U. Rao
L. A. Ruth
T. M. Torkos

DOE
OFFICE OF FOSSIL ENERGY
FE-72
19901 Germantown Road
Germantown, MD 20874-1290
F. M. Glaser

DOE
OFFICE OF VEHICLE AND ENERGY R&D
CE-151 Forrestal Building
Washington, DC 20585
R. B. Schulz

ELECTRIC POWER RESEARCH INSTITUTE
P.O. Box 10412
3412 Hillview Avenue
Palo Alto, CA 94303
W. T. Bakker
J. Stringer

EUROPEAN COMMUNITIES JOINT RESEARCH CENTRE
Petten Establishment
P.O. Box 2
1755 ZG Petten
The Netherlands
M. Van de Voorde

IDAHO NATIONAL ENGINEERING & ENVIRONMENTAL LABORATORY
P. O. Box 1625
Idaho Falls, ID 83415
B. H. Rabin

LAWRENCE LIVERMORE NATIONAL LABORATORY
P.O. Box 808, L-325
Livermore, CA 94550
W. A. Steele

NATIONAL MATERIALS ADVISORY BOARD
National Research Council
2101 Constitution Avenue
Washington, DC 20418
K. M. Zwilsky

OAK RIDGE NATIONAL LABORATORY
P.O. Box 2008
Oak Ridge, TN 37831
T. M. Besmann
P. T. Carlson
J. M. Crigger **(4 copies)**
R. R. Judkins
R. A. Lowden
D. P. Stinton
V. M. Vaubert

OFFICE OF NAVAL RESEARCH
Code 431, 800 N. Quincy Street
Arlington, VA 22217
S. G. Fishman

REMAXCO TECHNOLOGIES, INC.
1010 Commerce Park Drive
Suite I
Oak Ridge, TN 37830
R. D. Nixdorf

SHELL DEVELOPMENT COMPANY
WTC R-1371
P.O. Box 1380
Houston, TX 77251-1380
W. C. Fort

TENNESSEE VALLEY AUTHORITY
Energy Demonstration & Technology
MR2N58A
Chattanooga, TN 37402-2801
C. M. Huang

THE JOHNS HOPKINS UNIVERSITY
Materials Science & Engineering
Maryland Hall
Baltimore, MD 21218
R. E. Green, Jr.

THE MATERIALS PROPERTIES COUNCIL, INC.
United Engineering Center
345 E. Forty-Seventh Street
New York, NY 10017
M. Prager

THE NORTON COMPANY
High Performance Ceramics Division
Goddard Road
Northborough, MA 01532-1545
N. Corbin

UNION CARBIDE CORPORATION
Linde Division
P.O. Box 44
175 East Park Drive
Tonawanda, NY 14151-0044
Harry Cheung

UNITED TECHNOLOGIES RESEARCH CENTER
MS 24, Silver Lane

East Hartford, CT 06108
K. M. Prewo

UNIVERSITY OF LOUISVILLE
Dept of Chemical Engineering
Speed Scientific School
Louisville, KY 40292
T. L. Starr

UNIVERSITY OF NORTH DAKOTA
Energy and Environmental Research Center
15 North 23rd Street
Grand Forks. ND 56202
J. P. Hurley

UNIVERSITY OF TENNESSEE
Dept of Materials Science and Engineering
Knoxville, TN 37996-2200
P. K. Liaw

UNIVERSITY OF WASHINGTON
Department of Materials Science and Engineering
101 Wilson, FB-10
Seattle, WA 98195
T. G. Stoebe

VIRGINIA POLYTECHNIC INSTITUTE & STATE UNIVERSITY
Department of Materials Engineering
Blackburg, VA 24601
K. L. Reifsnider

WESTERN RESEARCH INSTITUTE
365 N. 9th Street
P.O. Box 3395
University Station
Laramie, WY 82071
V. K. Sethi

WESTINGHOUSE ELECTRIC CORPORATION
Research and Development Center
1310 Beulah Road
Pittsburgh, PA 15235-5098
S. C. Singhal